Charge Transfer Control of Emergent Magnetism at SrMnO₃/LaMnO₃ Interfaces

Jan Philipp Bange, Vladimir Roddatis, Leonard Schüler, Fryderyk Lyzwa, Marius Keunecke, Sergei Lopatin, Vitaly Bruchmann-Bamberg, and Vasily Moshnyaga*

Emergent phases at the interfaces in strongly correlated oxide heterostructures display novel properties not akin to those of constituting materials. The interfacial ferromagnetism in $(LaMnO_3)_m/(SrMnO_3)_n$ $(LMO)_m/(SMO)_n$ superlattices (SLs) with antiferromagnetic bulk LMO and SMO layers is believed to be a result of the interfacial charge transfer (CT). By using in situ optical ellipsometry, it is demonstrated directly that CT and emergent magnetism in $(LMO)_m/(SMO)_n$ SLs are controlled by the LMO/SMO thickness ratio, chosen as $m/n = 1$ and 2. The enhanced CT in SLs with $m/n = 2$ favors the high-T_C emergent ferromagnetism with $T_C = 350–360$ K, whereas the reduced CT in $m/n = 1$ SLs suppresses it yielding $T_C = 300$ K. A complex dependence of the saturation magnetization as a function of interface density $\Lambda = (m + n)^{-1}$ with minima at $\Lambda = 0.11$ ($m/n = 2$) and $\Lambda = 0.25$ ($m/n = 1$) was observed and rationalized by the competition of ferromagnetic and antiferromagnetic contributions, originating from the volume of LMO and SMO layers as well as from the LMO/SMO interfaces. The role of epitaxy stress and MnO_6 octahedral tilts in the emergent magnetic behavior is discussed.

1. Introduction

Heterostructures of strongly correlated oxides provide a rich material platform for searching and tuning of emergent interfacial magnetic and electric phenomena[1–4] not present in the constituting layers. As the interplay of charge, spin, and lattice degrees of freedom[5] is believed to control phase transitions in bulk correlated materials, their interfacial reconstructions, should serve as guiding mechanisms for emergent phenomena. In particular, the charge transfer (CT)/leakage at the interface[6,7] with a following electronic reconstruction of them was thought to be intimately coupled to the formation of emergent phases. The $(LaMnO_3)_m/(SrMnO_3)_n$ (LMO_m/SMO_n) SLs can be viewed as one of the most intensively studied oxide heterostructures.[8,9] A long-term interest to them was motivated by the observations of interfacial or emergent ferromagnetism,[10–14] associated with the chemically sharp LMO(top)/SMO(bottom) interfaces.[10] Very recently, we reported a high temperature emergent ferromagnetic phase with Curie temperature $T_C = 360$ K at the SMO/LMO interfaces,[15] originated from the interfacial CT from the electron-rich LMO to the electron-poor SMO layers.

An important but rather rarely addressed question is whether CT can be additionally influenced or controlled by the growth design of SLs, e.g. by tuning the thickness ratio of constituting layers. Garcia–Barriocanal et al.[7] have demonstrated that charge leakage in $(LaMnO_3)_m/(SrTiO_3)_n$ (LMO_m/STO_n) SLs, indicated by the formation of Ti^{3+} within the STO layers, is favored in the SLs with a large thickness ratio LMO_{17}/STO_2 and is suppressed when this ratio is small LMO_{17}/STO_{12}. Moreover, the LMO layers in SLs with a large thickness ratio (17/2) were found to be relaxed but those in SLs with small ratio (7/5) were coherently strained. Likely, a correlation between the CT and strain state in the LMO/STO SLs could be envisioned. In addition, it is known that magnetic properties of, e.g., LMO_6/SMO_4 SLs,[13] can be influenced by the epitaxy strain actuated by the chosen substrate, i.e., STO, LSAT, or $LaAlO_3$ (LAO). Namely, a small tensile strain in case of STO ($a_{STO} = 0.3905$ nm) or an almost strain-free state for the lattice matched LSAT ($a_{LSAT} = 0.3868$ nm) both promote ferromagnetism. In contrast, a compressive strain produced by the LAO substrate ($a_{LAO} = 0.3787$ nm) suppresses ferromagnetic ground state. However, the development of emergent magnetic phenomena in a wide range of LMO_m/SMO_n compositions and layer thicknesses as well as the correlations between the lattice structure and strain state of SLs are far from being well understood. Moreover, a possibility to control CT by growth design

J.P. Bange, L. Schüler, M. Keunecke, V. Bruchmann-Bamberg, V. Moshnyaga
Erstes Physikalisches Institut
Georg-August-Universität Göttingen
Friedrich-Hund-Platz 1 37077, Göttingen, Germany
E-mail: vmosnea@gwdg.de
V. Roddatis
GFZ German Research Centre for Geosciences
Helmholtz Centre Potsdam
Telegrafenberg, 14473 Potsdam, Germany
F. Lyzwa
National Synchrotron Light Source II
Brookhaven National Laboratory
New York 11973, USA
S. Lopatin
Core Lab King Abdullah University of Science and Technology
Thuwal 23955, Saudi Arabia

ADVANCED
SCIENCE NEWS
www.advancedsciencenews.com

ADVANCED
MATERIALS
INTERFACES
www.advmatinterfaces.de

and by tuning the SL architecture, e.g., by changing digital numbers "m", "n" and the "m/n" ratio in LMO/SMO SLs, was not addressed so far.

Here, we report a detailed study of magnetism in the LMO_m/SMO_n SLs, grown by metalorganic aerosol deposition (MAD) technique[16] on the STO(100) substrates. A systematic change of the layer thicknesses (n = 3, 4, 5, 6, 8, and 10) and of the LMO/SMO thickness ratio (m/n = 1 and 2) in these digital SLs was performed, allowing us to disclose the corresponding changes in the magnetism as a function of interface density as well as to relate these changes to the modification of the characteristic CT length, deduced from in situ optical ellipsometry.[17] Namely, the CT at the SMO(top)//LMO(bottom) interfaces was found to be controlled by the m/n ratio, which as well influences the emerging magnetism significantly.

2. Sample Preparation and Experimental Details

The $[LMO_m/SMO_n]_K$ SLs on STO(100) substrates with m/n = 1 and 2, called in the following SL1 and SL2, respectively, with the bilayer thickness, $\Lambda = m + n$ = 6–20, and repetition number of bilayers, K = 10, were grown using MAD technique as described in details.[15] The growth of SLs has been monitored in situ by optical ellipsometry as presented in **Figure 1**, where the thickness (D) and time (t) dependences of the ellipsometric phase shift angle, $\Delta(D = vt)$, are shown for representative 10/5 and 5/5 SLs. Within the LMO layers one can see a linear increase of the phase shift, Δ, in time/thickness with an almost constant phase shift rate, $d\Delta/dD$ = 0.3° u.c.$^{-1}$ In contrast, within the SMO layers a nonmonotonic behavior was observed with pronounced changes of the $d\Delta/dD$ rate within all SMO layers. The insets in Figure 1 with a zoomed view of the phase shift rate behavior demonstrate a sudden increase up to $d\Delta/dD$ = 0.5° u.c.$^{-1}$ occurs within the first 1–2 u.c. of the growing SMO layer. Further on, the rate drops down to small values $d\Delta/dD$ = 0.1° u.c.$^{-1}$ The observed here ellipsometric $\Delta(D)$ behavior, being in qualitative agreement with our previous results,[15] was characteristic for all SL1 and SL2 sample series. However, the details of the phase shift rate thickness behavior within the SMO layers close to the interfaces in SL1 and SL2 samples were found to be different and will be analyzed below.

Global structural characterization of SLs was performed by X-ray diffraction (XRD) and X-ray reflection (XRR) using a Bruker D8 diffractometer with Cu-K$_\alpha$ radiation. XRD and XRR patterns were simulated by ReMagX program.[18] Microscopic characterization was done using an FEI environmental Transmission Electron Microscope (ETEM) Titan 80–300. TEM
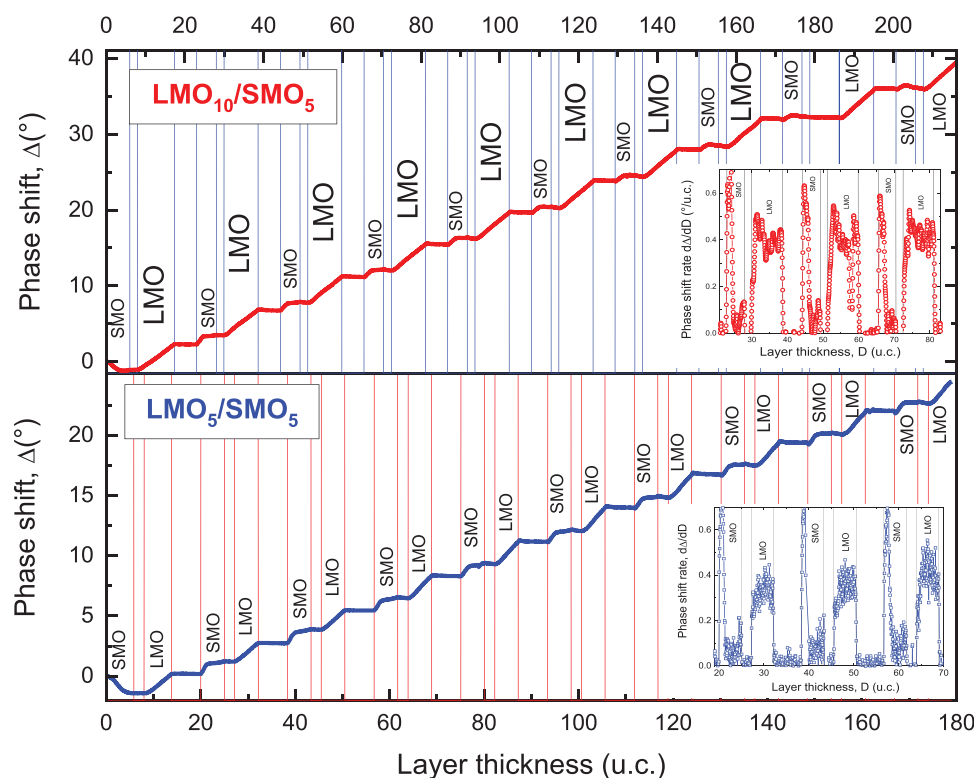
Figure 1. Ellipsometric phase shift angle, Δ, as a function of layer thickness, D, measured in situ during the growth of LMO_{10}/SMO_5 (top panel, red curve) and LMO_5/SMO_5 (bottom, blue) superlattices (SLs). The measured $\Delta(t)$ diagrams were renormalized to $\Delta(D = v \times t)$ dependences, using the known constant deposition rate v = 0.3 u.c. s^{-1}, independently verified by X-ray reflection and transmission electron microscopy (TEM) data. The vertical lines marked the opening and closing of LMO and SMO liquid channels. One can see an almost linear $\Delta(D)$ behavior for LMO layers and a nonmonotonous behavior for SMO layers caused by the charge transfer (CT) from the underlying LMO into the growing SMO layer.[15] The insets show the zoomed views of the phase shift rate, $d\Delta/dD$, as a function of layer thickness, which, being proportional to the electronic density in the layer,[15] illustrates the in situ CT across the interface from the LMO into the SMO and an increased electron concentration within the first two u.c. of SMO layers close to the SMO(top)/LMO(bottom) interface (see also Figure S1, Supporting Information).[20]

**ADVANCED
SCIENCE NEWS**
www.advancedsciencenews.com

**ADVANCED
MATERIALS
INTERFACES**
www.advmatinterfaces.de

lamellas were prepared in the [100] and [110] directions using a Thermofischer (former FEI) Helios UC focused ion beam instrument with a beam energy of 30 kV. A final cleaning step was performed at low energy (2 kV). A detailed study of crystal structure, including the quantitative analysis of the MnO_6 octahedral tilts in the LMO layers, is presented.[19] Magnetization was measured by using a SQUID magnetometer (MPMS XL, Quantum Design) for temperatures, $T = 5–400$ K and applied magnetic fields, $B = 0–5$ T, aligned parallel to the film surface.

3. Structure and Lattice Strain in the SLs

The high-angle annular dark field scanning transmission electron microscopy (HAADF-STEM) images of two representative SL1 (5/5) and SL2 (10/5) samples are shown in Figure S1 (Supporting Information).[20] It demonstrates epitaxially grown LMO and SMO layers with flat and atomically sharp interfaces. Additionally, a high structural quality of layers and interfaces as well as of the whole SL architecture is supported by the measurements and simulations of XRR and XRD (see Figures S2 and S3, Supporting Information[20]). The thicknesses of the LMO and SMO layers, determined from the XRR, as well as the simulated from XRD values of out-of-plane lattice parameters for individual SMO and LMO layers are presented in **Table 1**. One can see a good correspondence between the nominal layer thicknesses (n, m) and those experimentally measured (n_{exp}, m_{exp}) by TEM and XRR (bilayer thickness) with a deviation between them not exceeding 2–3%. Moreover, the XRD-determined averaged c-axis lattice parameters in SLs, C_{av}, allowed us to estimate the stress states in the LMO and SMO layers and compare the overall stress state of these two series of SLs. One can see from Table 1 that the C_{av} values are almost the same for all samples with the same m/n ratio. However, they differ sizably between the SL1 and SL2 series, having different LMO/SMO thickness ratio, i.e., $C_{av}(SL1) = 0.382$ nm and $C_{av}(SL2) = 0.3845$ nm. Moreover, from the simulations of the XRD patterns (Figures S2 and S3, Supporting Information) one can evaluate the c-axis lattice parameters of the individual layers, C_{LMO} and C_{SMO}, and calculate the theoretical values of the average $C_{av.th.}$-lattice parameters in SLs as $C_{av.th.} = (m \times C_{LMO} + n \times C_{SMO})/(m + n)$, which were then compared with the measured C_{av}-values (see Table 1). For the SL1 and SL2 sample series one gets $C_{av.th.}(SL1) = (0.3882 + 0.3750)/2 = 0.3816$ nm and $C_{av.th.}(SL2) = (2 \times 0.3892 + 0.3722)/3 = 0.3835$ nm. A pretty good correspondence between the measured and theoretically calculated values of the averaged C_{av}-lattice parameters in the SLs reflects the different mass ratio of LMO and SMO in them and confirms that the LMO/SMO thickness ratios are close to the nominal values for all SL samples in the "$m/n = 1$" and "$m/n = 2$" series.

Further, the SMO layers in SLs are stronger in-plane tensile stressed as the LMO layers. Namely, the evaluated tensile stress in the SMO layers $\varepsilon = (C_{SMO,f} - C_{SMO,bulk})/C_{SMO,bulk}$, is equal to $\varepsilon_{SMO}(SL1) = -1.7\%$ and $\varepsilon_{SMO}(SL2) = -2.1\%$ ($c_{SMO,bulk} = 0.3805$ nm[21]). In contrast, the stress in the LMO layers in SLs, i.e., $\varepsilon = (c_{LMO,f} - c_{LMO,bulk})/c_{LMO,bulk}$, is estimated to be significantly smaller because the pseudocubic lattice parameter of the LMO layers and also of single LMO films is very close to the in-plane lattice parameter of the STO substrate; the resulting stress values are $\varepsilon_{LMO}(SL1) = -0.6\%$ and $\varepsilon_{LMO}(SL2) = -0.3\%$. Neverthe-

Table 1. The data of X-ray reflectivity (XRR) and X-ray diffraction (XRD) for all superlattices (SLs). Individual thicknesses of layers d_{SMO} and d_{LMO} were obtained from simulations by using of ReMagX program[18] and the mean out-of-plane lattice parameters, C_0, from the measured XRD patterns. n_{exp} and m_{exp} are evaluated from the XRR and XRD thicknesses of SMO and LMO layers, respectively.

| $(LMO_m/SMO_n)_{10}$		XRR		XRD			
m	n	D_{SMO} [nm]	D_{LMO} [nm]	$\Lambda = D_{LMO} + D_{SMO}$ [nm]	C_{av} [nm]	m_{exp}	n_{exp}
3	3	1.1	1.1	2.3	0.382	2.9	2.9
4	4	1.5	1.5	3.0	0.382	3.9	4.0
5	5	1.78	2.0	3.8	0.382	5.1	4.8
6	6	2.0	2.2	4.2	0.382	5.7	5.8
10	10	3.5	3.9	7.4	0.382	10	9.2
6	3	1.2	2.2	3.5	0.385	5.8	3.1
8	4	1.5	3.0	4.5	0.384	7.8	3.9
10	5	1.94	4.0	5.94	0.384	10.2	5.2
12	6	2.3	4.7	7.0	0.385	11.2	6.1
20	10	3.8	8	11.8	0.385	20.5	10.0

less, one can see a difference in the LMO stress states between the SL1 and SL2 series – in the latter LMO layers are much less strained. Interestingly, the overall stress values, given as a sum of the LMO and SMO stresses, i.e., $\varepsilon_{SL}(SL1) = -1.7$ to $0.6 = -2.3\%$ and $\varepsilon_{SL}(SL2) = -2.1$ to $0.3 = -2.4\%$, are very similar in the SL1 and SL2 samples because the LMO and SMO layers reveal opposite changes.

4. Magnetism

In **Figure 2**, we present the temperature and field dependences of the magnetic moment, $M(T)$, measured by SQUID for two representative SL2 (12/6) and SL1 (6/6) samples. One can see a complex behavior with two ferromagnetic transitions with low (T_{C1}) and high (T_{C2}) Curie temperatures. The T_C values were determined from the position of the minimum of the function $TCM(T) = (1/M) \times (dM/dT)$ also shown in the inset of Figure 2a. Such $M(T)$ curves with two ferromagnetic transitions were found to be characteristic for all other SL samples in the present study. Moreover, one can see also characteristic differences between the 12/6 (SL2) and 6/6 (SL1) samples, indicating stronger magnetic properties in the 12/6 (SL2) sample. Namely, $T_{C2} = 355$ K obtained for the 12/6 SL exceeds considerably the $T_{C2} = 300$ K in the 6/6 SL (see Figure 2a) and, moreover, the saturation magnetization in the 12/6 SL exceeds that for the 6/6 SL by more than two times (see Figure 2b). Further, the 6/6 SL shows a significantly larger coercive field $H_c = 1.8$ kOe compared to the $H_c = 0.5$ kOe measured for the 12/6 SL. Finally, both 12/6 and 6/6 SLs display a pronounced exchange bias field, $H_{EB} = 90$ and 130 Oe, respectively. Concluding, the temperature and field dependent magnetization with two ferromagnetic transitions, shown in Figure 2 for the two chosen SLs, are typical for all other SL2 and SL1 samples in the present study. Moreover, the $M(T)$ and $M(H)$ dependences in SL2 samples reproduce the recently published results on SLs with $m/n = 2$.[15]

In **Figure 3**, we summarized the results of the temperature and field dependent SQUID magnetization for all present
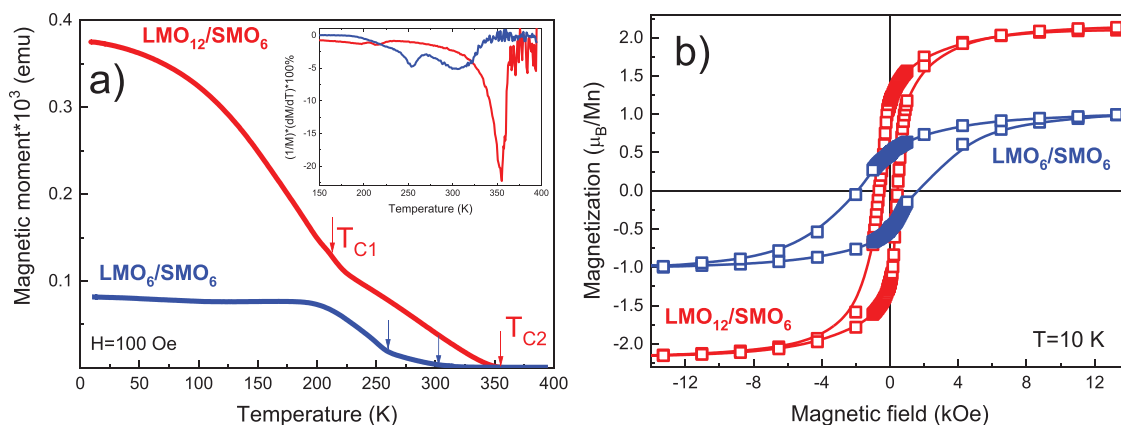
Figure 2. Temperature (a) and magnetic field (b) dependences of magnetization for representative superlattices (SLs) with $m/n = 2(12/6)$ and $m/n = 1(6/6)$. The inset in (a) shows the $TCM(T)$ function, from which the Curie temperatures of a low-T_{C1} and high-T_{C2} ferromagnetic phases were determined.
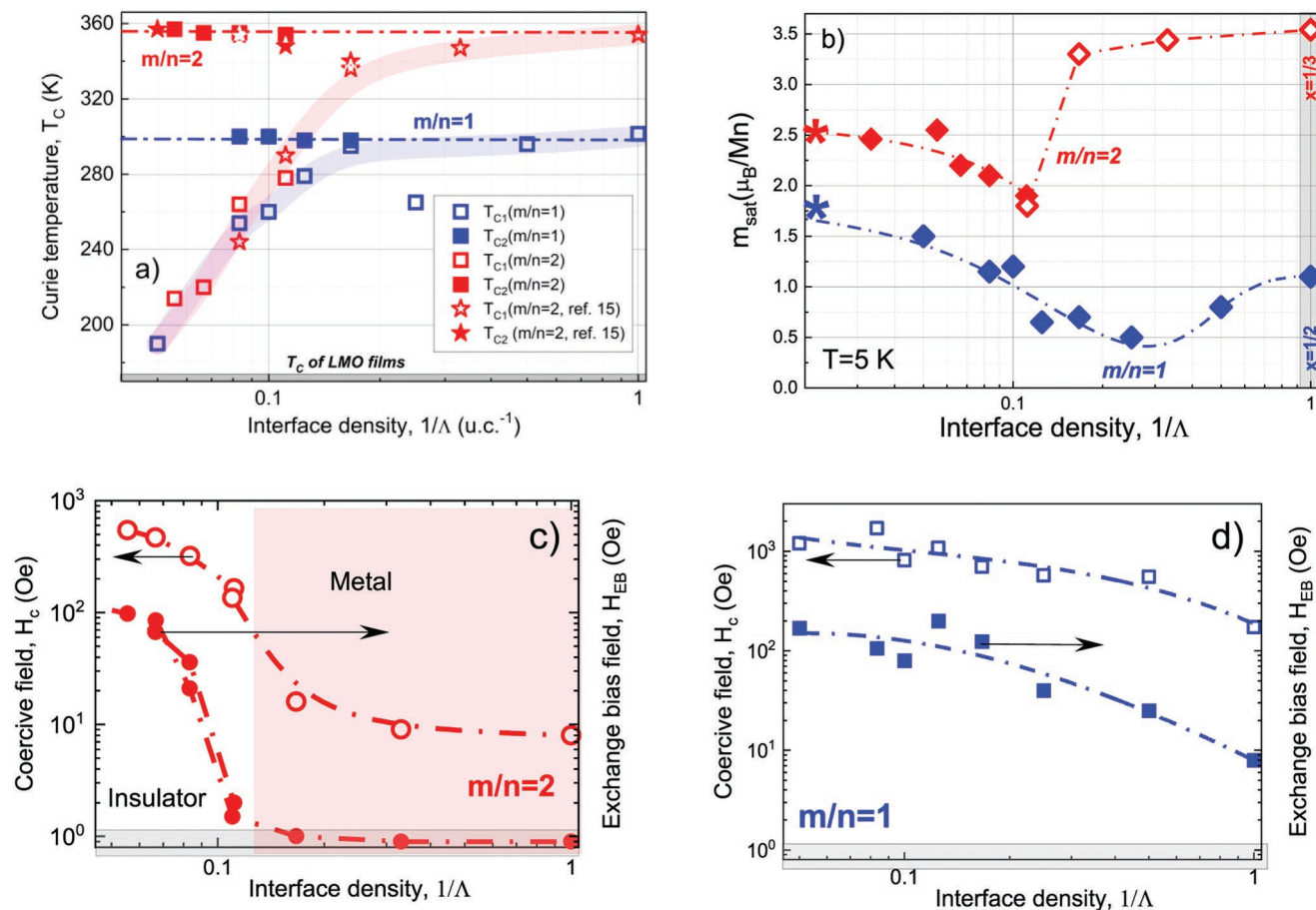
Figure 3. Magnetic properties of LMO/SMO superlattices (SLs) as a function of interface density. a) Ferromagnetic transition temperatures: low-T_{C1} (open symbols) and high-T_{C2} (close symbols). Symbols with blue and red color refer to SLs with $m/n = 1$ and $m/n = 2$. The gray shaded area indicates the T_C of a single LMO film. All other curves are guides to the eye. b) Saturation magnetization, m_{sat} measured at $T = 5$ K. Blue and red symbols refer to SLs with $m/n = 1$ and 2, respectively. All curves are guides to the eye. Symbols (*) marked the expected m_{sat} values for the weighted volume LMO contributions in SLs with $m/n = 2$ and 1, respectively, dominating at $1/\Lambda = 0$. Open symbols in b) denote data taken.[15]; coercive fields, H_c, (open red symbols) and exchange bias fields, H_{EB}, (closed red symbols) of the LMO/SMO SLs with $m/n = 2$ (c) and $m/n = 1$ (d). All curves are guided to the eye. Horizontal dashed segments in (c) and (d) represent the measurement accuracy of the exchange bias field $\delta H_{EB} = 1$ Oe. The values at $\Lambda = 1$ relate to the single LSMO films with Sr-doping $x = 1/3$ (c) and $x = 1/2$ (d).

SL1 and SL2 samples, having different bilayer thicknesses, $\Lambda = m + n$, and interface densities, $1/\Lambda = (m + n)^{-1}$. In addition, we have included the data from ref. [15] to get a complete overview. As one can see from Figure 3a, the T_{C1} values decrease with decreasing the $1/\Lambda$ for both types of SLs and for low interface densities, $1/\Lambda < 0.1$, they approach $T_C = 160$–170 K of single LMO films with a thickness $D = 20$–40 nm.[15,22] This indicates that the low-T_{C1} transition originates from a "volume-like" LMO ferromagnetic contribution, which progressively increases with increasing the LMO thickness and decreasing interface density $(1/\Lambda)$ in SLs. Note that the FM ground state in epitaxial LMO films, in contrast to the AFM ground state in bulk LMO, is known to be stabilized by the epitaxy stress.[23] In contrast, T_{C2} values, being almost independent on the interface density $1/\Lambda$ within both SL series, characterize the onset of the interfacial emergent FM phase.[1] Remarkably, we observed that a high-T_{C2} emergent ferromagnetism does depend on the m/n ratio as the determined values of $T_{C2} = 355$–360 K for the SL2 samples exceed significantly the $T_{C2} = 300$ K for the SL1 samples. This suggests that the CT, which was supposed to be the reason of the formation of the emergent FM phase,[15] could be influenced by the LMO/SMO thickness ratio.

In Figure 3b, the saturation magnetization $m_{sat}(5K)$ of SLs is plotted as a function of the interface density $1/\Lambda$; the data of single $La_{1-x}Sr_xMnO_3$ (LSMO) films as boundary cases for SL1 ($x = 1/2$) and SL2 ($x = 1/3$) are added for comparison at $1/\Lambda = 1$. Apparently, one can see a pronounced $m_{sat}(1/\Lambda)$ dependence with generally reduced values, $m_{sat} = 0.5$–2.5 μ_B Mn^{-1}, in SLs compared to those for optimally doped bulk LSMO[24] or single LSMO films.[15] Interestingly, a minimum in the $m_{sat}(1/\Lambda)$ dependence can be seen at $1/\Lambda = 0.11$ ($\Lambda = 9$ u.c.) for 6/3 SL2 and at $1/\Lambda = 0.25$ ($\Lambda = 4$ u.c.) for the 2/2 SL1. Note that the pronounced minimum for the SL2 samples appears in the vicinity of the transition from an LSMO-like ferromagnetic behavior in SLs with very thin SMO layers ($n = 1, 2$ u.c.) to an SL-specific magnetism for $n \geq 3$, which is manifested by the competition of the interface and bulk-like contributions from the LMO and SMO layers. Indeed, large $m_{sat} = 3.3$–3.5 μ_B Mn^{-1} comparable with those in the optimally doped bulk LSMO as well as a metallic behavior was observed[15] for SL2 samples with $n = 1, 2$. At $n = 3$ a metal-insulator transition occurs in the SL2 system and leads to a strong reduction of m_{sat} probably due to the increase of the antiferromagnetic (AFM) contribution in SLs. This is further supported by a drastic and steep enhancement of coercive field, H_c, and appearance of the exchange bias field, H_{EB}, for SL2 samples with $n > 3$, shown in Figure 3c. For the $m/n = 1$ SLs a less pronounced minimum in the $m_{sat}(1/\Lambda)$ dependence seen in the 2/2 SL probably also reflects a transition from a bulk-like behavior similar to the half-doped LSMO for $n < 2$ to an SL governed magnetism for $n > 2$. However, at $\Lambda = 4$ no MI transition takes place because even the reference half-doped LSMO films are rather insulating and, likely, electronically inhomogeneous. The absence of an MI transition in SL1 samples is additionally illustrated by a monotonous $H_c(1/\Lambda)$ and $H_{EB}(1/\Lambda)$ behavior shown in Figure 3d.

Thus, the complex $m_{sat}(1/\Lambda)$ dependences for SL2 and SL1 samples (see Figure 3b) with reduced saturation magnetization and their minima indicate the presence and even the dominance of an AFM phase in SLs with very thin LMO and

SMO layers ($n = 2$–6) and correspondingly large interface density $1/\Lambda = 0.08$–0.25 (u.c.)$^{-1}$. Especially pronounced is the AFM phase within the SL1 samples, which displays very low values $m_{sat} = 0.4$–1.2 μ_B Mn^{-1}. The AFM contributions originate most probably from the SMO layers, which start to acquire their bulk magnetic properties for thicker layers $n > 3$.[15] Another source of the AFM contribution could be provided by the LMO(top)/SMO(bottom interface) as according to polarized neutron scattering[15] the first 3 u.c. of the LMO grown on top of the SMO also possess an AFM ground state with a nearly zero magnetization. This means that SLs with a thicker SMO ($n \geq 3$ u.c.) and LMO ($2n > 6$ u.c.) layers and relatively high interface density $1/\Lambda = 0.1$–0.2 (u.c.)$^{-1}$ display lower values of m_{sat}, dominated mostly by the interfacial FM contribution, as the AFM ordered LMO and SMO layers likely do not contribute to m_{sat}. By further increasing the layer thickness and further reducing the interface density the LMO finally becomes an FM and m_{sat} of an SL increases. For an SL with thick LMO and SMO layers and vanishingly small interface density $(1/\Lambda \rightarrow 0)$, which as well results in a vanishingly small interfacial FM contribution, the m_{sat} should approach the volume-like LMO value as bulk SMO being in the AFM ground state do not contribute to m_{sat}. Nevertheless, the coercive field and exchange bias fields remain large (see Figure 3c,d) at this limit because of the AFM ground state of the SMO. Taking $m_{sat}(LMO) = 3.7$ μ_B Mn^{-1} measured in single LMO films, the extrapolated to $1/\Lambda \rightarrow 0$ values should approach $m_{sat}(SL1) = M_{sat}(LMO) \times 1/2 = 1.85$ μ_B Mn^{-1} and $m_{sat}(SL2) = m_{sat}(LMO) \times 2/3 = 2.47$ μ_B Mn^{-1}. A good agreement with the measurements in Figure 3b proves the validity of this model. Thus, the thickness dependent AFM/FM competition in the LMO and SMO layers and a decrease of the contribution from interfacial emergent ferromagnetism, both occurring by decreasing the interface density, are at the origin of the non-monotonic magnetic behavior shown in Figure 3b.
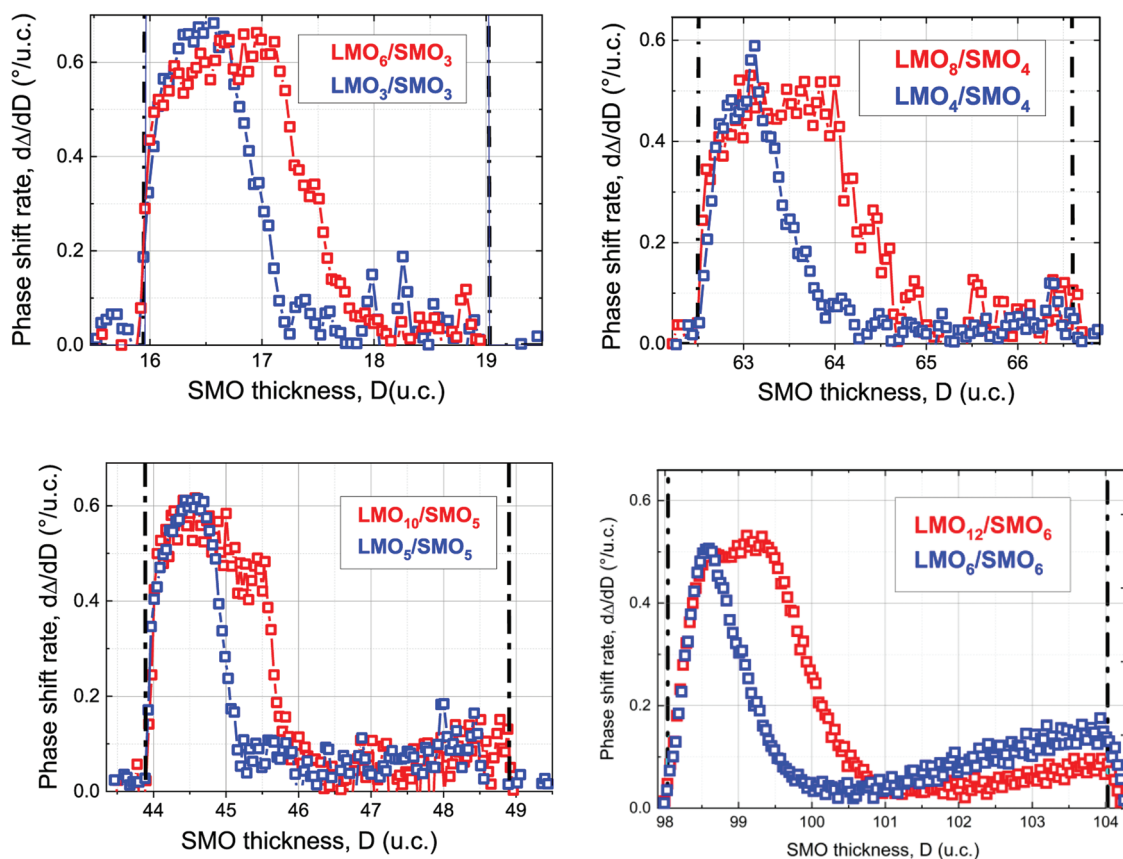
5. Charge Transfer

The main result of the present study is that the emergent magnetism in LMO$_m$/SMO$_n$ SLs can be influenced by the "m/n" thickness ratio of the constituting layers: the large "$m/n = 2$" ratio favors ferromagnetism and results in a high-T_C emergent phase while the small "$m/n = 1$" ratio suppresses it. Taking into account that the reason of the emergent magnetism is a CT across the SMO/LMO interface[15] and considering previous results of Garcia–Barriokanal et al.,[7] one can suggest that CT is enhanced in the SL2 and is suppressed in the SL1 samples. To examine this issue we have analyzed the ellipsometry time (t)/thickness (D) diagrams measured in situ during the growth of SL2 and SL1 samples and shown exemplified for 5/5 and 10/5 SLs in Figure 1. Our analysis is based on the phase shift rate, $d\Delta/dD$, which reflects the electron density and its change in the growing film.[15] Indeed, the thin LSMO films[15] and LMO layers in SLs (see Figure 1) with well-defined electronic properties show a linear increase of delta during growth. This can be described by a phase shift rate $d\Delta/dD$, which stays constant during the layer growth and provides information on the electronic properties of the growing layer as will be discussed in the following. Note, that ellipsometry as an optical/infrared reflection technique is

**ADVANCED
SCIENCE NEWS**

www.advancedsciencenews.com

**ADVANCED
MATERIALS
INTERFACES**

www.advmatinterfaces.de

generally sensitive to electronic properties of a material probed at a special excitation photon energy,[25] here $E = 1.96$ eV (light wavelength $\lambda = 632.8$ nm). To elaborate the relationship between the phase shift rate and charge density we modeled the in situ ellipsometry signal of a growing multilayer using the Fresnel equations[25] and have shown that it is determined by the complex refractive index of the top layer (see Supporting Information[20]), which in turn is related to its electronic properties. With refractive indices of single LSMO films with Sr doping $0 < x < 1$, evaluated from measurements of in situ ellipsometry (see Figure S4, Supporting Information[20]), the values of phase shift rate $d\Delta/dD$ were determined from the Fresnel equations for very thin LSMO layers with $D \le 12$ u.c., which are relevant for the SLs (see Figure S5, Supporting Information[20]). One can see a characteristic dependence the phase shift rate on "x" with a pronounced maximum of $d\Delta/dD$ for optimally doped LSMO, which explains the enhanced phase shift rate at the SMO(top)/LMO(bottom) interfaces due to the CT.[15] The simulations also reproduce the relatively large values of $d\Delta/dD = 0.3°$ u.c.$^{-1}$, observed in electron-rich LMO (see Figure 1) and small $d\Delta/dD = 0.1°$ u.c.$^{-1}$ seen in the electron-poor SMO layers. It is important to note that the photon energy $E = 1.96$ eV, used in our ellipsometry setup, fits almost exactly the excitation energy ($E = 2$ eV) of the intersite $Mn^{3+} \rightarrow Mn^{3+}$ optical transitions.[26] Considering the fact that spectral weight of these transitions is very sensitive to Sr-or Ca-doping[27] or in other words to the Mn^{3+}/Mn^{4+} ratio, the

sensitivity of the ellipsometric phase shift rate to the electron/hole density in manganites can be rationalized.

Being aware that we cannot directly determine the amount of charge transferred across the interface, we carried out a comparative analysis of the phase shift rate within the SMO layers in all present SL samples with $m/n = 1, 2$ with the main aim to quantify the differences in the CT length λ_{TF} within these two series of SLs. In **Figure 4**, we present a comparison of the phase shift rate within the SMO layers in SL2 and SL1 samples, having the same thickness of SMO, e.g. we compare the 10/5 and 5/5 SLs. One can see that all studied SL2 samples (red symbols) display a sizably broader distribution of the phase shift rate or, in other words, of charge spreading into the SMO layers than that measured in the SL1 (blue symbols). For example, the CT length, λ_{TF}, estimated in the 6/6 and 12/6 SLs was $\lambda_{TF} = 1$ and 2 u.c., respectively. For other SLs with thinner SMO layers ($n = 3, 4, 5$ u.c.) the progressively smaller λ_{TF} values were obtained. Interestingly, the relative difference in $\delta\lambda_{TF}$ between the SL1 and SL2 samples normalized to the thickness of SMO layers $n = 3, 4, 5, 6$, i.e., $\delta\lambda_{TF}/n$, or charge spreading within SMO was found to be nearly the same for all SL2 samples, i.e., ≈ 0.5 u.c./3 = 0.166; ≈ 0.65 u.c./4 = 0.165; ≈ 0.8 u.c./5 = 0.16, and 1 u.c./6 = 0.166. These data indicate, likely, a very similar "effective electron doping" for all SL2 samples, having different SMO thickness, "n," but the same ratio $m/n = 2$. This supports our suggestion that the emerging high-


Figure 4. Ellipsometric phase shift rate, $d\Delta/dD$, within the SMO layers for superlattices (SLs) with $m/n = 1$ (blue) and $m/n = 2$ (red) evidences a broadened charge distribution within the SMO layers for the $m/n = 2$ SLs and indicates an enhancement of charge transfer (CT) in these SLs.

**ADVANCED
SCIENCE NEWS**

www.advancedsciencenews.com

**ADVANCED
MATERIALS
INTERFACES**

www.advmatinterfaces.de

T_{C2} ferromagnetic phase is caused by the enhanced CT within the SMO layers in $m/n = 2$ SLs.

An additional way to detect the CT across the interface can be the estimation of the oxidation states of the Mn ions inside the LMO and SMO layers in SLs. Indeed, the electrostatic mismatch at the SMO/LMO interface with the formally charged $(La-O)^{+1}/(Mn-O_2)^{-1}$ layer and formally neutral $(Sr-O)^0/(Mn-O_2)^0$ layer, could be relaxed by the CT. Assuming that LMO loses electrons and the SMO acquires them, this should lead to the modified oxidation states of $Mn^{3+\delta}$ within the LMO and $Mn^{4-\delta}$ (SMO). Moreover, also the layers above and below the interface could be involved because of the charge redistribution within the bilayer. The most accurate tool for estimation of Mn oxidation states was shown[28,29] to be electron energy loss spectroscopy (EELS) at the O-K edge and determination of the energy distance between the $O-K_b$ and $O-K_a$ peaks, $\Delta E_{ba} = E_{Oka} - E_{OKb}$. This procedure, compared to the L_3/L_2 ratio[30,31] measured at the $Mn-L_{2,3}$ edge, is less sensitive to the noise. The high resolution EELS behavior for the 6/6 and 12/6 SLs, shown in **Figure 5**a,b, respectively, demonstrates how the spectra close

to the O-K and $Mn-L_{2,3}$ edges are distributed along the growth direction of SLs. One can see qualitative differences between the LMO and SMO layers in SLs in agreement with our previous results.[15] The SMO layers are manifested by an energy shift of the O-K edge (mostly of the central peak) and by the intensity changes of the $Mn-L_{2,3}$ edge due to the changes in the L_3/L_2 ratio. The obtained EELS spectral behavior is generally similar to that reported for bulk manganites and thin films previously.[28–31]

In Figure 5c,d, we present the EELS spectra at the O-K edge, measured in the middle of the LMO (Figure 5c) and SMO (Figure 5d) layers for 12/6 and 6/6 SLs as well as for the reference LMO/STO and SMO/STO single films. The measured EELS spectra contain typical features, called $O-K_a$ and $O-K_b$ peaks,[28,29] the energy distance between which ΔE_{ba} has been demonstrated to be very sensitive to the oxidation states of Mn ions[28] as well as for stress state of the films as demonstrated for the SMO films grown on different substrates.[29] The peaks were fitted by Gauss curves as shown in Figure 5c,d and the values ΔE_{ba} were determined. As one can see in Figure 5e, by comparing
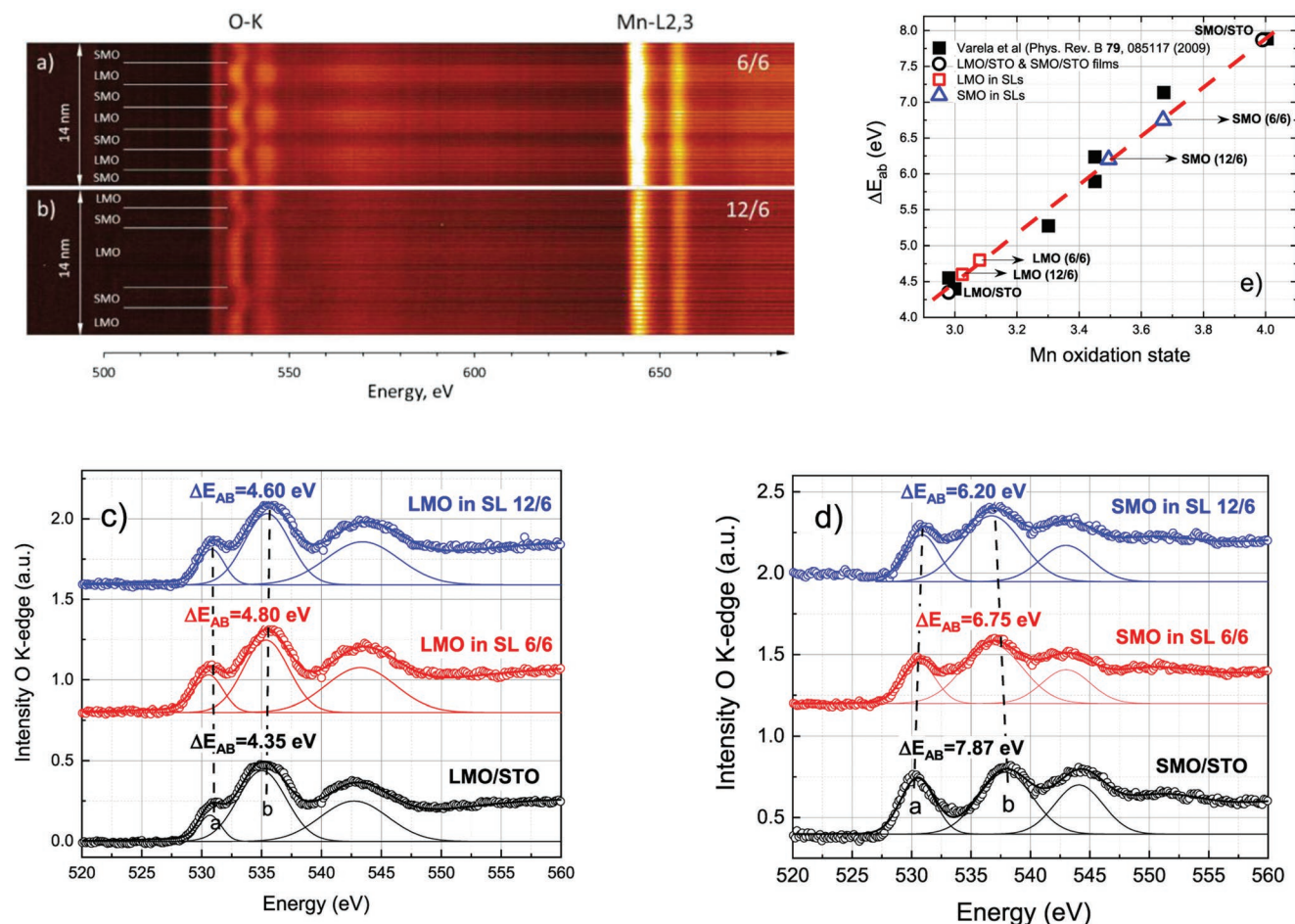
Figure 5. The distribution of the electron energy loss spectroscopy (EELS) spectra in the vicinity of the O-K and $Mn-L_{2,3}$ edges along the growth direction in 6/6 (a) and 12/6 superlattices (SLs) (b). The EELS spectra around the O-K edge, measured inside the LMO (c) and SMO (d) layers in 12/6 (blue) and 6/6 (red) SLs as well as in single LMO/STO and SMO/STO films (black curves) grown by metalorganic aerosol deposition (MAD). The spectra were fitted with Gauss lines; shown are only first three lines marked by thin lines and the sum curve of all peaks (thick lines). The energy distance between the $O-K_b$ and $O-K_a$ peaks, $\Delta E = E(O-K_b) - E(O-K_a)$, was determined. e) A superposition of our results on the data of Varela et al.[28] obtained for $La_{1-x}Ca_xMnO_3$ manganites.

**ADVANCED
SCIENCE NEWS**

www.advancedsciencenews.com

**ADVANCED
MATERIALS
INTERFACES**

www.advmatinterfaces.de

the data on our samples with the data on La$_{1-x}$Ca$_x$MnO$_3$ measured by Varela et al.,[28] the reference LMO/STO and SMO/STO films do possess the nominal oxidation states, i.e., Mn^{3+} and Mn,[4] respectively. The values of ΔE_{ba} obtained in the middle of the LMO and SMO layers in SLs, i.e., "far away" from interfaces (see Figure 5c,d, respectively) indicate modified oxidation states. Namely, oxidation states of Mn in LMO layers inside the SLs are relatively close to Mn^{3+}, i.e., $V_{LMO}(12/6) = +3.05$ and $V_{LMO}(6/6) = +3.1$. In contrast, those for the SMO layers deviate significantly from Mn^{4+}: $V_{SMO}(12/6) = +3.5$ and $V_{SMO}(6/6) = +3.7$. Note, the obtained here small deviations from the nominal Mn^{3+} in LMO layers, being close to the uncertainty of ± 0.15 given by the L_3/L_2 method,[30] cannot be reliably determined by it. However, the determined Mn oxidation states in SMO layers exceed this uncertainty. In principle, the oxidation state of Mn in SMO films can be also influenced by strain-induced oxygen deficiency as demonstrated by Agrawal et al.[29] Comparing the ΔE_{ba} values for SMO layers in our SLs with their results, similar oxidation states should be resulted from the 2.6% and 3.7% strain in the SMO layers for the 6/6 and 12/6 SLs, respectively. However, according to the XRD the stress values in SMO layers are significantly smaller, i.e., 1.7% (6/6) and 2.1% (12/6) and, moreover, the oxygen deficiency was not detected in our SMO layers. Thus, we conclude that the stress alone cannot lead to the observed strong deviations of Mn oxidation states in SMO. The most probable reason seems to be the in situ LMO-to-SMO CT, followed by a redistribution of the electron density within the underlying LMO layers.

6. Discussion

We performed a systematic study of the magnetism in LMO$_m$/ SMO$_n$ SLs ($m/n = 1,2$; $m, n = 2$–10 u.c.) and demonstrated its correlation with electronic/structural reconstructions at the interfaces analyzed by in situ ellipsometry and ex situ EELS. The observed high-T_C emergent magnetic behavior in $m/n = 2$ SLs was assigned to an enhanced CT within ≈ 2 u.c. at the SMO/ LMO interfaces. The latter were optically/electronically modeled by assuming the formation of an optimally doped LSMO ($x = 1/3$) phase at the interface. Emergent behavior observed here and elsewhere[15] in the MAD grown LMO$_{2n}$/SMO$_n$ SLs is quite different from that found in the MBE grown SLs,[10,32] which possess strongly asymmetric interfaces and do not show high-T_C emergent phase. Here, we would like to note that interfaces in MAD-grown SLs are flat and quite similar—the SMO(top)/ LMO(bottom) is atomically sharp with an XRR roughness, $\sigma_{SMO/LMO} = 1$ u.c., and the LMO(top)/SMO(bottom) looks less sharp ($\sigma_{LMO/SMO} = 1.5$ u.c.). According to the ellipsometry and polarized neutron scattering[15] the emergent high-T_C FM phase is located at the sharp SMO/LMO interface, which can be modeled by electronic properties of optimally doped LSMO. This indicates that the electronic reconstruction is responsible for the emergent high-T_C FM phase. A chemically less sharp and likely intermixed LMO/SMO interface with accompanying chemical disorder is not relevant for high-T_C magnetism. Moreover, assuming only a chemical intermixing at the interfaces, a half-doped interfacial LSMO ($x = 0.5$) phase should be present in both $m/n = 1$ and 2 SLs. This, however, contradicts (see

Figure 3a) the experimentally observed systematic difference in the emergent ferromagnetism in these SLs.

The estimated from the ellipsometry CT lengths into the SMO in SLs, e.g. $\lambda_{TF}(6/6) = 1$ u.c. and $\lambda_{TF}(12/6) = 2$ u.c., can be related to the EELS-determined average Mn oxidation states V_{LMO} and V_{SMO} assuming a redistribution of the electron density within the layers as follows: $V_{LMO} = [3(m - \lambda_{TF}) + 4\lambda_{TF}]/m = 3 + \lambda_{TF}/m$ and $V_{SMO} = [4(n - \lambda_{TF}) + 3\lambda_{TF}]/n = 4 - \lambda_{TF}/n$. For the LMO in 12/6 and 6/6 SLs one gets a similar Mn oxidation sates, $V_{LMO}(12/6) \sim V_{LMO}(6/6) = +3.17$, because of a factor of two larger CT length for the 12/6 SL than that for the 6/6 SL. These values are in line with those measured by EELS (see Figure 5e) in the middle of the LMO layers in SLs, $=+3.1(12/6)$. Moreover, the average Mn oxidation states in SMO are: $V_{SMO}(12/6) = 3.67$ and $V_{SMO}(6/6) = 3.83$, which also agree quite good with the EELS-determined values for SMO, i.e., $+3.5$ (12/6) and $+3.7$ (6/6). Thus, the control of CT by the "m/n" thickness ratio, its relevance for the emerging magnetism and its enhancement in the $m/n = 2$ SLs is qualitatively supported both by in situ ellipsometry and ex situ EELS measurements.

Another important issue is whether the CT and stress state in the studied SLs are related to each other. For example, as was shown by Garcia–Barriocanal et al.[7] the CT leads to almost fully relaxed LMO layers in the LMO/STO SLs. As we have shown above in Section 3 the $m/n = 1$ and 2 SLs possess a very similar overall tensile stress state with SMO layers much more strained than those of LMO. It is interesting to note that an enhanced CT in the SLs with $m/n = 2$ and decrease of stress in the LMO layers likely correlate with each other. At this point we speculate that the transferred electrons into the SMO help to relax the LMO by reducing the tetragonal distortion by means of MnO$_6$ octahedral tilt mechanism. According to the recent study of Meyer et al.[19] the main structural difference between the present SL1 and SL2 samples is the existence of octahedral tilts in the LMO layers within the $m/n = 2$ SLs and their absence in the $m/n = 1$ SLs. The presence of tilts is consistent with an increased averaged C_{av}-lattice parameter measured for the SL2 samples (see Table 1) and, hence, with a decreased tetragonal distortion in them. Note, that Kan et al.[33] also reported an example of anisotropic strain relief in the SrRuO$_3$ films by engineering of octahedral rotations at the interface between SrRuO$_3$ and GdScO$_3$ substrate. However, the microscopic scenario of the strain relief by octahedral rotations and the role of charge and orbital reconstructions in it still needs a detailed theoretic description.

We believe the m/n ratio could affect the magnitude of the CT due to following mechanisms: a) mechanic strain or "mass" effect—the larger the mass ratio the larger the influence of LMO on SMO; b) structural effect actuated by different types of interfaces, i.e., Mn–O–Mn tilt-mismatched in the $m/n = 2$ SLs and mismatch-free the $m/n = 1$ SLs; and c) electrostatic mismatch effect quantified by the difference in capacities of charge reservoirs (electron-rich LMO and electron-poor SMO) might directly drive the interfacial CT. In addition, we would like to note that such a direct "electrostatic mismatch" effect on CT, being proceeded already during the growth at high temperatures, $T_{sub} = 900$–950 °C, plays a dominant role in our opinion. The role of other two factors (a) and (b) and their casual relationship in the realization of CT seems to be not clear up to now.

ADVANCED
SCIENCE NEWS

www.advancedsciencenews.com

ADVANCED
MATERIALS
INTERFACES

www.advmatinterfaces.de

7. Conclusions

The LMO_m/SMO_n SLs series with $m/n = 1$ and 2 were grown on STO(100) substrates by means of MAD technique in the range of individual layer thicknesses m, $n = 2$–10. The high-T_{C2} emergent ferromagnetic phase was controlled by the LMO/SMO thickness ratio, m/n. The latter was shown to influence the CT from the LMO(donor) to the SMO(acceptor) layer as was demonstrated by the in situ optical ellipsometry and supported by the atomically resolved EELS data. An intimate connection between spin reconstructions at the interfaces, CT, and lattice strain is suggested as a guiding mechanism for controlling magnetism in correlated heterostructures.

Supporting Information

Supporting Information is available from the Wiley Online Library or from the author.

Conflict of Interest

The authors declare no conflict of interest.

Data Availability Statement

The data that support the findings of this study are available on request from the corresponding author. The data are not publicly available due to privacy or ethical restrictions.

[1] H. Y. Hwang, Y. Iwasa, M. Kawasaki, B. Keimer, N. Nagaosa, Y. Tokura, *Nat. Mater.* **2012**, *11*, 103.

[2] J. Chakhalian, J. W. Freeland, A. J. Millis, C. Panagopoulos, J. M. Rondinelli, *Rev. Mod. Phys.* **2014**, *86*, 1189.

[3] C. A. F. Vaz, F. J. Walker, C. H. Ahn, S. Ismail-Beigi, *J. Phys.: Condens. Matter* **2015**, *27*, 123001.

[4] F. Hellman, A. Hoffmann, Y. Tserkovnyak, G. S. D. Beach, E. E. Fullerton, C. Leighton, A. H. MacDonald, D. C. Ralph, D. A. Arena, H. A. Dürr, P. Fischer, J. Grollier, J. P. Heremans, T. Jungwirth, A. V. Kimmel, B. Koopmans, I. N. Krivorotov, S. J. May,

[5] E. Dagotto, *Science* **2005**, *309*, 257.

[6] B. R. K. Nanda, S. Satpathy, *Phys. Rev. B* **2010**, *81*, 224408.

[7] J. Garcia-Barriocanal, F. Y. Bruno, A. Rivera-Calzada, Z. Sefrioui, N. M. Nemes, M. Garcia-Hernandez, J. R.-Z., G. R. Castro, M. Varela, S. J. Pennycook, C. leon, J. Santamaria, *Adv. Mater.* **2010**, *22*, 627.

[8] P. A. Salvador, A.-M. Haghiri-Gosnet, B. Mercey, M. Hervieu, B. Raveau, *Appl. Phys. Lett.* **1999**, *75*, 2638.

[9] C. Adamo, X. Ke, P. Schiffer, A. Soukiassian, M. Warusawithana, L. Maritato, D. G. Schlom, *Appl. Phys. Lett.* **2008**, *92*, 112508.

[10] S. J. May, A. B. Shah, S. G. E. te Velthuis, M. R. Fitzsimmons, J. M. Zuo, X. Zhai, J. N. Eckstein, S. D. Bader, A. Bhattacharya, *Phys. Rev. B* **2008**, *77*, 174409.

[11] S. Dong, R. Yu, S. Yunoki, G. Alvarez, J.-M. Liu, E. Dagotto, *Phys. Rev. B* **2008**, *78*, 201102.

[12] C. Aruta, C. Adamo, A. Galdi, P. Orgiani, V. Bisogni, N. B. Brookes, J. C. Cezar, P. Thakur, C. A. Perroni, G. De Filippis, V. Cataudella, D. G. Schlom, L. Maritato, G. Ghiringhelli, *Phys. Rev. B* **2009**, *80*, 140405.

[13] H. Yamada, P.-H. Xiang, A. Sawa, *Phys. Rev. B* **2010**, *81*, 014410.

[14] S. Smadici, B. B. Nelson-Cheeseman, A. Bhattacharya, P. Abbamonte, *Phys. Rev. B* **2012**, *86*, 174427.

[15] M. Keunecke, F. Lyzwa, D. Schwarzbach, V. Roddatis, N. Gauquelin, K. Mueller-Caspary, J. Verbeeck, S. J. Callori, F. Klose, M. Jungbauer, V. Moshnyaga, *Adv. Funct. Mater.* **2020**, *30*, 1808270.

[16] M. Jungbauer, S. Hühn, R. Egoavil, H. Tan, J. Verbeeck, G. Van Tendeloo, V. Moshnyaga, *Appl. Phys. Lett.* **2014**, *105*, 251603.

[17] F. Lyzwa, P. Marsik, V. Roddatis, C. Bernhard, M. Jungbauer, V. Moshnyaga, *J. Phys. D: Appl. Phys.* **2018**, *51*, 125306.

[18] S. Macke, A. Radi, J. E. Hamann-Borrero, A. Verna, M. Bluschke, S. Brück, E. Goering, R. Sutarto, F. He, G. Cristiani, M. Wu, E. Benckiser, H.-U. Habermeier, G. Logvenov, N. Gauquelin, G. A. Botton, A. P. Kajdos, S. Stemmer, G. A. Sawatzky, M. W. Haverkort, B. Keimer, V. Hinkov, *Adv. Mater.* **2014**, *26*, 6554.

[19] D. Meyer, V. Roddatis, J. P. Bange, S. Lopatin, M. Keunecke, D. Metternich, U. Ross, I. V. Maznichenko, S. Ostanin, I. Mertig, V. Radisch, R. Egoavil, I. Lazić, V. Moshnyaga, H. Ulrichs, arXiv:2009.14532v3 **2020**, https://arxiv.org/abs/2009.14532v3.

[20] See Supplemental Material at https://onlinelibrary.wiley.com/doi/full/.

[21] O. Chmaissem, B. Dabrowski, S. Kolesnik, J. Mais, D. E. Brown, R. Kruk, P. Prior, B. Pyles, J. D. Jorgensen, *Phys. Rev. B* **2001**, *64*, 134412.

[22] P. Ksoll, R. Mandal, C. Meyer, L. Schüler, V. Roddatis, V. Moshnyaga, *Phys. Rev. B* **2021**, *103*, 195120.

[23] J. Roqueta, A. Pomar, L. Barcells, C. Frontera, S. Valencia, R. Abrudan, B. Bozzo, Z. Konstantinovic, J. Santiso, B. Martinez, *Cryst. Growth Des.* **2015**, *15*, 5332.

[24] A. Urushibara, Y. Moritomo, T. Arima, A. Asamitsu, G. Kido, Y. Tokura, *Phys. Rev. B* **1995**, *51*, 14103.

[25] H. Fujiwara, *Spectroscopic Ellipsometry. Principles and Applications*, Wiley, Weinheim **2007**.

[26] K. Tobe, T. Kimura, Y. Okimoto, Y. Tokura, *Phys. Rev. B* **2001**, *64*, 184421.

[27] J. H. Jung, K. H. Kim, T. W. Noh, E. J. Choi, J. Yu, *Phys. Rev. B* **1998**, *57*, R11043.

[28] M. Varela, M. P. Oxley, W. Luo, J. Tao, M. Watanabe, A. R. Lupini, S. T. Pantelides, S. J. Pennycook, *Phys. Rev. B* **2009**, *79*, 085117.

[29] P. Agrawal, J. Guo, P. Yu, C. Hébert, D. Passerone, R. Erni, M. D. Rossell, *Phys. Rev. B* **2016**, *94*, 104101.

[30] Z. L. Wang, J. S. Yin, Y. D. Jiang, *Micron* **2000**, *31*, 571.

[31] H. Tan, J. Verbeeck, A. Abakumov, G. Van Tendeloo, *Ultramicroscopy* **2012**, *116*, 24.

[32] A. B. Shah, Q. M. Ramasse, S. J. May, J. Kavich, J. G. Wen, X. Zhai, J. N. Eckstein, J. Freeland, A. Bhattacharya, J. M. Zuo, *Phys. Rev. B* **2010**, *82*, 115112.

[33] D. Kan, Y.u. Wakabayashi, H. Tajiri, Y. Shimakawa, *Phys. Rev. B* **2016**, *94*, 024112.

A. K. Petford-Long, J. M. Rondinelly, N. Samarth, I. K. Schuller, A. N. Slavin, M. D. Stiles, O. Tchernyshyov, B. L. Zink, *Rev. Mod. Phys.* **2017**, *89*, 025006.